Journal of Materials Chemistry A

ROYAL SOCIETY OF CHEMISTRY

PAPER

View Article Online
View Journal | View Issue

Cite this: J. Mater. Chem. A, 2025, 13, 31279

Organic dual-ion batteries with low-temperature operability and structural reinforcement

Chen Wang, [a] Suyash Oka, [a] Mohd Avais, [b] Dimitris C. Lagoudas,[bc] James G. Boyd,[c] Micah J. Green [ab] and Jodie L. Lutkenhaus *[ab]

Lithium-ion batteries have been widely used in portable electronic devices for many years. However, these batteries still face significant challenges in harsher and more complex environments such as electric vehicles, aerospace, subsea operations, and power grid systems. Two of the most significant limitations of current lithium-ion batteries are their weak mechanical strength and poor low-temperature performance. To address these limitations, this study leverages carbon fiber weave current collectors to deliver high mechanical strength and a dual-ion organic battery configuration to improve low-temperature operability. A copolymer of 2,2,6,6-tetramethyl-piperidenyloxyl-4-yl methacrylate and glycidyl methacrylate (PTMA-*co*-GMA) and naphthalene tetracarboxylic dianhydride-derived polyimide (PNTCDI) are used as active materials for the positive and negative electrodes, respectively, on the carbon fiber weave current collectors to fabricate structural battery electrodes. Low-temperature structural organic batteries using carbon fiber reinforcement have not yet been demonstrated until now. The carbon fiber (CF) current collectors offer similar capacity performance and better cycling stability compared to metal ones, making CF current collectors a promising option for structural organic batteries. Furthermore, the study uses a lithium bis(trifluoromethane)sulfonimide (LiTFSI) and diglyme-based low-temperature electrolyte to fabricate dual-ion cells that could operate at low temperatures. The battery exhibited a capacity of 76 mAh g^{-1} at 1C current, maintaining operability up to 10C current, and delivering 1000 W kg^{-1} specific power down to −40 °C. The battery maintained 85% capacity at 0 °C and 55% capacity at −40 °C. Interestingly, the battery showed near-zero capacity decay while cycling at low temperatures. Overall, this study demonstrates the potential of combining high mechanical strength and low-temperature operability in one battery. The proposed approach represents an important step forward in developing organic batteries with multi-functionality, empowering their use in a broader range of applications in extreme environments.

Received 27th February 2025
Accepted 3rd August 2025

DOI: 10.1039/d5ta01626f

rsc.li/materials-a

1. Introduction

Energy storage applications including electric vehicles, power grids, aerospace vehicles, and subsea vehicles have harsh and diverse requirements for the multifunctional performance of batteries, including resilience to mechanical stress and extreme temperature, as well as strict safety demands.[1–7] Structural batteries that have high mechanical strength, elastic modulus, and toughness for resisting mechanical failure and deformation have emerged as promising solutions to this challenge.[3,8–13] In practice, structural batteries may offer substantial mass savings for electric vehicles[14] and potentially lay the foundation for electric aircraft.[3] Previously reported structural batteries rely highly on carbon fibers as load-bearing materials.[15–19] One early approach was the use of carbon fiber reinforced plastics (CFRP), embedding thin-film lithium-ion batteries or pouch cells into CFRP laminates.[20,21] Unfortunately, this approach is additive – not integrative.

An integrative approach is that of embedding carbon fibers (CFs) into the batteries' components, such as with CF-based structural electrodes. Martha *et al.* coated $LiFePO_4$ (LFP) onto CFs to make structural electrodes with a capacity of 165 mAh g^{-1} at 1C current.[16] Yao *et al.*, Lu *et al.*, and Hagberg *et al.* also reported different lithium-metal-oxide coated CFs as structural electrodes.[15,17,22] The Asp group reported a full structural battery with LFP-coated CFs as the positive electrode, pristine CFs as the negative electrode, glass fiber as the separator, and a bisphenol A ethoxylate dimethacrylate-based solid electrolyte.[23] They obtained a tensile strength of 25.4 GPa without outer reinforcements. In contrast, the capacity of the battery only reached 38.4 mAh g^{-1} (calculated based on active material mass) at 0.05C (1C = 170 mA g^{-1}) current, yielding only 22.5%

[a]Artie McFerrin Department of Chemical Engineering, Texas A&M University, College Station, TX, 77843, USA. E-mail: jodie.lutkenhaus@tamu.edu; Tel: +1(979)-845-2682
[b]Department of Materials Science & Engineering, Texas A&M University, College Station, TX, 77843, USA
[c]Department of Aerospace Engineering, Texas A&M University, College Station, TX, 77843, USA

of the cell's theoretical capacity. In a previous study from our group, Oka *et al.* studied the mechanical properties of PTMA-*co*-GMA coated carbon fiber weave electrodes.[24] CF composites of epoxy and redox-active polymer PTMA-*co*-GMA showed an ultimate tensile strength of 320 MPa and a Young's modulus of around 16 GPa, with CF being responsible for carrying the mechanical load. The PTMA-*co*-GMA structural electrode was paired with graphite and with lithium metal foil to create a full cell. The highest power measured was >5000 W kg^{-1} at 25C, and the highest energy was 364 Wh kg^{-1} at 0.1C. That study did not examine fully organic structural cells, and the lowest temperature investigated was only −20 °C.

Current commercial lithium-ion batteries show a sharp loss of capacity below 0 °C and are rarely recommended for use below −20 °C.[25–27] To meet the requirements of aerospace or subsea applications, low-temperature operability is also crucial for lithium-ion batteries. Most reports on low-temperature batteries have primarily focused on electrolyte development. Ein-Eli *et al.*, Plichta *et al.*, and others studied different electrolytes with a solvent mixture of ethylene carbonate (EC) and other linear carbonates or esters.[28–32] EC is a crucial component of commercial electrolytes because it helps to passivate the graphite anode and form a stable solid-electrolyte interface (SEI).[33] However, a major drawback of EC is its high melting point of 34–37 °C,[34] which renders the resulting electrolytes unsuitable for low-temperature applications. Consequently, significant research efforts have been devoted to the development of EC-free electrolytes. Xu *et al.* reported a dioxolane-based electrolyte for a battery with nano lithium titanate (LTO) and lithium nickel manganese cobalt oxides (NCM) electrode materials, which received promising performance down to −80 °C.[35] All-organic (non structural) polymer-based active materials were also reported in low-temperature batteries. Dong *et al.* reported a cell with PTPAn cathode, polyimide (PI) anode, and 2 M lithium bis(trifluoromethane) sulfonimide (LiTFSI) in ethyl acetate as electrolyte.[36] The cell demonstrated almost 50% of the room temperature capacity at −50 °C and 5C. The cell showed an average discharge potential of around 1.2 V (0 °C) to 1.0 V (−70 °C). The capacity at 5C (specific power around 500 W kg^{-1}) was 91 mAh g^{-1} (25 °C) to 46 mAh g^{-1} (−50 °C), which corresponds to a specific energy of 103 Wh kg^{-1} (25 °C) to 13.5 Wh kg^{-1} (−50 °C). Jiang *et al.* reported a calcium ion battery with PTPAn cathode, PI anode, and 1 M $CaClO_4$ in acetonitrile as the electrolyte.[37] The cell showed a lower discharge voltage of 0.9 to 1 V. At 2C (0.2 A g^{-1}, specific power around 190 W kg^{-1}), the cell showed a capacity of 83.4 mAh g^{-1} (25 °C) to 50.9 mAh g^{-1} (−50 °C), which corresponds to 82.9 Wh kg^{-1} (25 °C) to 47.3 Wh kg^{-1} (−50 °C). Taken together, the bulk of low-temperature battery studies have centered on metal-ion or lithium-metal battery chemistries and none were structural.

Organic redox-active polymers as active materials are gaining increasing interest due to the greater availability of raw materials, high charge/discharge current, and environmental friendliness.[38–42] In this work, we chose the copolymer of 2,2,6,6-tetramethyl-piperidenyloxyl-4-yl methacrylate and glycidyl methacrylate (PTMA-*co*-GMA) as the positive active material and naphthalene tetracarboxylic dianhydride-derived polyimide (PNTCDI) as the negative active material. The redox-active group in PTMA-*co*-GMA is the (2,2,6,6-tetramethylpiperidin-1-yl)oxyl (TEMPO) group. The TEMPO nitroxide radical can be oxidized into an oxoammonium cation and is thus paired with an anion from the electrolyte.[38,39] PTMA-*co*-GMA is a p-type polymer with a working potential of around 3.6 V (*vs.* Li^+/Li) and a theoretical capacity of 110 mAh g^{-1}, depending on GMA content. Nakahara *et al.* first studied the electrochemical performance of PTMA and observed a practical capacity of 77 mAh g^{-1} and excellent stability.[38] Kim *et al.* reported that the capacity of PTMA could reach 111 mAh g^{-1} with high carbon ratio in the electrode.[43] However, one major drawback of PTMA is its dissolution in the electrolyte during long-term cycling. To address this problem, Wang *et al.* reported a cross-linkable copolymer, PTMA-*co*-GMA.[44] As for the negative active material, PNTCDI is a polyimide that has a theoretical capacity of 158 mAh g^{-1} and a working potential of around 2.4 V (*vs.* Li^+/Li).[45] PNTCDI is an n-type polymer for which the imide's carbonyl group is reduced to alkoxide ion and paired with lithium ions from the electrolyte. These polymers have never been used in low-temperature, structural organic batteries.

Dual-ion batteries store energy by exchanging cations at the anode, and anions at the cathode.[46] Inorganic, organic, and graphitic electrodes have been used in dual-ion batteries.[46–48] We hypothesized that, with PTMA-*co*-GMA (p-type polymer) and PNTCDI (n-type polymer) as active materials, the battery would work as a dual-ion cell, rather than the rocking-chair mechanism in traditional lithium-ion batteries. While charging, lithium-ions insert into the negative electrode (PNTCDI) and anions insert into the positive electrode (PTMA-*co*-GMA); while discharging, the ions are released back into the electrolyte. The dual-ion mechanism is useful for improving the low-temperature performance of the battery because it partly solves the sluggish desolvation and re-intercalation problem of lithium ions during discharge at the cathode.[1]

This work aims to develop a battery with high mechanical strength and low-temperature operability for potential use in extreme environments. To achieve high-strength electrodes, CF weave is chosen as the current collector onto which PTMA-*co*-GMA and PNTCDI are coated to comprise the positive and negative electrodes, respectively. The CF is expected to deliver a maximum strength of 4.2 GPa, and a modulus of 227 GPa, based on the manufacturer's data. For the battery to work at low temperatures an electrolyte with low melting point and high ionic conductivity is crucial. We utilize a low-temperature electrolyte consisting of 1 M LiTFSI in diglyme with 10 wt% fluorinated ethylene carbonate (FEC) to pair with the polymer-based electrodes. Diglyme has a low melting point and is reported to work well under low temperatures;[49] LiTFSI has high solubility, ionic conductivity, and stability; and FEC helps to form a better CEI. The resulting dual-ion, organic structural battery maintained 56% of its room temperature capacity at −50 °C and 1C current. It also shows minimal capacity decay after 300 cycles of charge discharge at −20 °C. The power of the resulting battery was exceptionally high (over 1000 W kg^{-1} down to −40 °C and 10C), from using the redox-active polymer

chemistry. This work reveals the creation and operation of a structural organic battery for low temperatures, integrating the mechanical properties of CF with the high power of the organic battery platform.

2. Materials and methods

2.1. Materials

1,4,5,8-Naphthalenetetracarboxylic dianhydride (NTCDA), 2,2,6,6-tetramethyl-4-piperidinyl methacrylate (TMPM) and 4-fluoro-2-oxo-1,3-dioxolane (FEC) were purchased from Tokyo Chemical Industry Co., Ltd. *P*-Phenylenediamine (*p*-PDA), glycidyl methacrylate (GMA), 1-methyl-2-pyrrolidinone (NMP), 2,2′-azobis-2-methylpropionitrile (AIBN), *m*-chloroperoxybenzoic acid (*m*-CPBA), lithium bis(trifluoromethane)sulfonimide (LiTFSI) and diglyme were purchased from Sigma-Aldrich Corporation. PVDF binder (M_w = 600 000 g mol^{-1}) and super P (conductive carbon) were purchased from MTI corporation. The carbon fiber weave used in this research was 3 K plain weave CF fabric, purchased from Fibre Glast Developments Corp. As listed by the manufacturer, the CF has a maximum strength of 4.2 GPa, a modulus of 227 GPa, and an elongation of 1.4%. CR2032-type coin cell cases made of SS316 stainless steel were purchased from MTI Corporation. CF was treated with acetone to remove the sizing on the fiber's surface and then dried at 80 °C for 12 h before use. All the other reagents and materials were used as received without further purification.

2.2. Preparation of PTMA-*co*-GMA

TMPM (5.0 g, 22 mmol) and 1% GMA (29 μL, 0.22 mmol) were dissolved in 10 ml toluene, and AIBN (0.11 g, 0.67 mmol) were added to initialize the radical polymerization; the mixture was reacted at 60 °C for 48 h. After the reaction, the mixture was filtered and washed with ethanol several times and dried under vacuum for 12 h to give PTMPM-*co*-GMA, a precursor of PTMA-*co*-GMA. Then, PTMPM-*co*-GMA (1.0 g, 4.4 mmol based on TMPM monomer) and 2 equivalents of *m*-CPBA (1.5 g, <77%) were dissolved in 10 ml dichloromethane; the reaction lasted for 3 h, and then the mixture was washed with water and 0.5 M sodium bicarbonate solution, respectively. The orange organic phase was separated from the aqueous phase. Twenty equivalents of hexane (v : v) were added to the separated organic phase to precipitate the solid. The mixture was vacuum-filtered, and the solid was dried at 50 °C for 24 h to receive orange PTMA-*co*-GMA powder. Gel permeation chromatography (GPC) was also performed; M_n = 18 800 g mol^{-1}, M_w = 42 200 g mol^{-1}, and $Đ$ = 2.28. EPR spectroscopy of PTMA-*co*-DMA was done to determine the radical content of the polymer and its actual theoretical capacity; the results are shown in Fig. S1.

2.3. Preparation of PNTCDI

2.7 g NTCDA and 1.1 g *p*-PDA were dissolved in 150 ml NMP and reacted under reflux for 6 h. After the reaction, the mixture was vacuum-filtered and washed with ethanol several times. Then the received solid was dried under vacuum at 120 °C for 12 h and then heated under argon at 300 °C for 12 h for complete polymerization and removal of any excess solvents. The PNTCDI sample was a reddish brown powder. The chemical structure of the as-prepared PNTCDI sample was characterized using Fourier transform infrared (FTIR) spectroscopy (JASCO FTIR-4600LE) (Fig. S2). In the FTIR spectrum, the strong adsorption peak of amine groups in *p*-PDA (around 3500 cm^{-1}) was not found in PNTCDI, which indicated complete imidization. Solid state $^{13}C\{^1H\}$ CP MAS NMR spectra were recorded at spinning rates of 11 kHz with a Bruker Avance-NEO solid-state NMR spectrometer (400 MHz) equipped with a standard two-channel 4 mm MAS probe head. The external reference was TMS. Cross-polarization (CP) experiments were carried out with the contact time of 1.2 ms, 900 ^{1}H-pulses (2.5 μs), the standard ppm15 pulse sequence for high-power (80 kHz) ^{1}H decoupling, and relaxation delays of 5 s. The $^{13}C\{^1H\}$ MAS NMR experiment was performed with HPDEC pulse program with 500 ^{13}C pulses of 2.0 μs and relaxation delays of 10 s. The spectrum (Fig. S3) revealed distinct signals around 120–140 ppm, attributed to aromatic or conjugated (C=C) carbons, and prominent peaks near 160 ppm (which are ascribed amide moieties) confirming the structure of polymer. GPC could not be performed on PNTCDI because it did not dissolve easily in known solvents.

2.4. Electrode preparation

To fabricate the positive electrode, PTMA-*co*-GMA (25 mg), Super P (20 mg), and PVDF (5.0 mg) were mixed in NMP with a weight ratio of 5 : 4 : 1. The resulting slurry was cast onto aluminum foil (for metal foil-based cells) and CF (for CF based cells) using an automated doctor blade. Then, the specimen was dried at room temperature for 12 h and heated to 175 °C for 3 h for crosslinking. The dried sample was cut into round discs to produce the electrodes. The loading of active material (PTMA-*co*-GMA) was 0.8 mg cm^{-2} for aluminum foil-based electrodes and 1 mg cm^{-2} for CF-based electrodes.

To fabricate the negative electrode, PNTCDI (35 mg), Super P (10 mg), and PVDF (5.0 mg) were mixed in NMP with a weight ratio of 7 : 2 : 1. The resulting slurry was coated onto copper foil (for metal foil-based cells) and CF (for CF-based cells) using an automated doctor blade. Then, the specimen was dried at 80 °C for 12 h. The dried sample was cut into round discs to produce the electrodes. The loading of active material (PNTCDI) was no less than 1 mg cm^{-2} for aluminum foil-based electrodes and CF-based electrodes.

2.5. Electrolyte preparation

Diglyme (anhydrous) and FEC were mixed under argon with a ratio of 9 : 1 (w : w) and then stored with 3 Å molecular sieves to remove any excess water. Then, LiTFSI was added into the mixed solution to prepare the 1 M LiTFSI low-temperature electrolyte. A commercial electrolyte (Sigma-Aldrich, 1 M $LiPF_6$ in ethylene carbonate and diethyl carbonate (EC/DEC = 1 : 1, v : v)) was used as received.

2.6. Characterization of the electrolyte

Symmetric lithium cells with the prepared electrolyte were used to test the electrochemical stability of the electrolyte. The

testing cells were CR2032-type coin cells with 12 mm diameter lithium foil as both electrodes, glass fiber separators (GF/A), and the electrolyte. The cell was then tested using linear sweep voltammetry (LSV) at a scan rate of 10 mV s^{-1} at different temperatures and reduction/oxidation potential limits. LSV was carried out on a Reference 600 Potentiostat (Gamry Instruments Inc.). To test the ionic conductivity of the electrolyte, a CR2032 coin cell case filled with the prepared electrolyte was subjected to electrochemical impedance spectroscopy (EIS) testing on a Reference 600 Potentiostat (Gamry Instruments Inc.). The DC voltage was 0 V (open circuit potential (OCP) of the cell), and an amplitude of 5 mV was applied as the excitation signal, and the frequency range was 100 kHz −0.1 Hz. The cell was tested at multiple temperatures. The ionic conductivity was calculated using the following formula:

$$\sigma = \frac{1}{R_b} \times K_{cell} = \frac{1}{R_b} \times \frac{l}{A} \quad (1)$$

Using the data given by MTI for the CR2032 coin cell, l = 0.266 cm and the inner diameter d = 1.65 cm. The calculated cell constant was K_{cell} = 0.124 cm^{-1}. The bulk resistance R_b was gathered using EIS.

2.7. Cell fabrication

Using the above-mentioned electrodes or lithium foil (for half cells), the low-temperature electrolyte, and glass fiber separators (GF/A), CR2032 cells were assembled under argon in a glove box with humidity and oxygen content lower than 3 ppm. In the prepared full cells, the capacity ratio of active materials in the positive and negative electrode was approximately 1.1 : 1.

2.8. Electrochemical characterization

Cyclic voltammetry (CV) profiles were collected at a scan rate of 0.2 mV s^{-1} using the prepared coin cell. For half cells, a polymer electrode (PTMA-*co*-GMA or PNTCDI) was used as the working electrode, and lithium foil acted as the reference and counter electrode. For full cells, the PTMA-*co*-GMA electrode was used as the positive electrode, and the PNTCDI electrode was used the negative electrode. The potential windows for testing were as follows: for PTMA-*co*-GMA half cell: 3.5–4.1 V (*vs.* Li^+/Li); for PNTCDI half cell: 1.85–3.1 V (*vs.* Li^+/Li); for full cells: 0.7–2.1 V, respectively. The galvanostatic charge–discharge (GCD) tests of the batteries were obtained using a BT2000 battery tester (Arbin Instruments) at different current densities (C-rates) in the same potential window as the CVs. The current densities and specific capacities were determined by the amount of PTMA-*co*-GMA (positive electrode active material). The temperature was controlled using an environmental testing chamber manufactured by Tenney Environmental. For EIS, the DC voltage was 1.4 V (around the discharge plateau voltage of the full cell), the AC amplitude was 5 mV, and the frequency range was 100 kHz–0.01 Hz.

3. Results and discussion

Because carbonate-based solvents used in commercial lithium-ion batteries freeze at low temperatures,[24] we selected an alternative solvent mixture for our electrolyte. Diglyme has a melting point of −64 °C,[50] which is significantly lower than the carbonate-based solvents (Table S1). FEC is often used as an additive for forming a thin and robust solid electrolyte interface (SEI), and was reported to improve battery performance at low temperatures.[51] In a previous work of our group, the CEI composition of PTMA and other TEMPO-derived redox-active polymers was studied in which we found that a CEI forming agent could improve the performance of PTMA electrodes.[52] Thus, a solution of 1 M LiTFSI in a mixture of 90% diglyme and 10% FEC (w : w) was prepared as the low temperature electrolyte (LTE). Fig. 1a shows a differential scanning calorimetry (DSC) thermogram for the LTE; no obvious peaks associated with melting or freezing were detected even at temperatures as low as −80 °C. This suggests that the LTE remains liquified at low temperatures.

Linear sweep voltammetry (LSV) was performed to determine the stable potential window at different temperatures (−50 °C to 24 °C) using symmetric lithium cells containing the LTE and a separator, Fig. 1b. All LSV tests were performed using a scan rate of 10 mV s^{-1} but with different reduction and oxidation potential limits, depending on temperature. At room temperature, the stability window of the LTE was 1.2–4.2 V (*vs.* Li^+/Li), which is similar to commercial lithium ion battery electrolyte (1 M $LiPF_6$ in EC/DEC (1 : 1), 1.3–3.9 V).[53,54] Moreover, the results of the LSV tests show that the potential window of stability widens as the temperature decreases. At −20 °C, a much wider stable potential window of 0.1–5.5 V was achieved, and at harsher conditions such as −50 °C, the window further widened to −0.8–6.4 V.

The ionic conductivity of the LTE at various temperatures was characterized using electrochemical impedance spectroscopy (EIS) of coin cells filled with the LTE in a blocking electrode configuration. Fig. 1c shows Nyquist plots of the LTE at different temperatures. In general, the impedance of the electrolyte increases as the temperature decreases. The resulting ionic conductivity of the LTE is shown in Fig. 1d, and the ionic conductivity of a commercial electrolyte (LB303, 1 M $LiPF_6$ in EC/DEC/DMC = 1 : 1 : 1) is also shown for comparison.[55] At room temperature the LTE showed an ionic conductivity of 6 mS cm^{-1}, which was lower than that of the commercial electrolyte. However, as the temperature dropped below −30 °C, the ionic conductivity of the commercial electrolyte declined to ~0.01 mS cm^{-1} at −40 °C. In contrast, the ionic conductivity of the LTE was much higher than that of the commercial electrolyte at low temperatures; for instance, the ionic conductivity of the LTE was 0.2 mS cm^{-1} even at −50 °C. These results show that the diglyme-based LTE has a low melting point, wide potential window, and high ionic conductivity at low temperatures. This shows that the LTE is more suitable for low-temperature batteries when compared to the commercial electrolyte LB303.

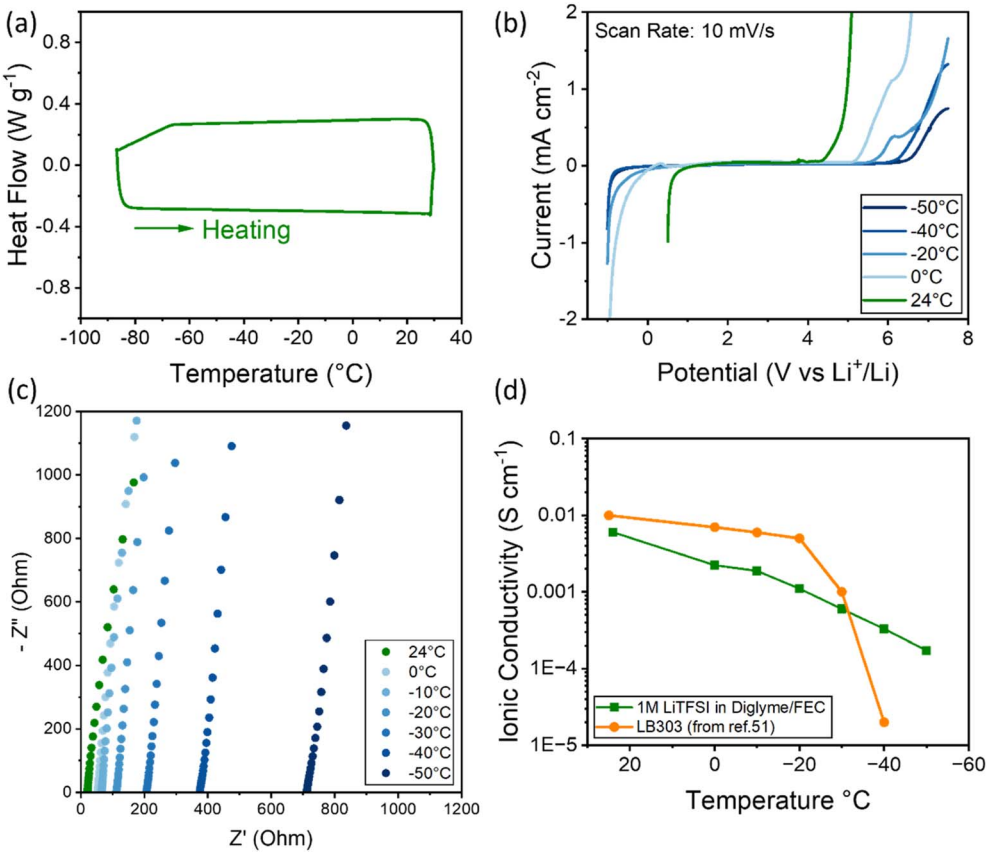

Fig. 1 (a) DSC thermogram of the low-temperature electrolyte (LTE) from −85 °C to room temperature at a scan rate of 10 °C min^{-1}. (b) Linear sweep voltammetry of the LTE in a symmetric lithium cell at varying temperatures at a scan rate of 10 mV s^{-1}. (c) Nyquist EIS plot of the LTE at different temperatures. (d) Ionic conductivity of the LTE at different temperatures; the ionic conductivity of LB303 (ref. 55) is shown for comparison.

As mentioned in the introduction, batteries with a "dual-ion" mechanism may overcome the problem of sluggish lithium ion desolvation during discharge[1] at low temperatures. Hence, PNTCDI and PTMA-*co*-GMA were selected as active materials for the negative and positive electrodes, respectively, of the dual-ion battery. In this work, the active materials were coated on CF (instead of aluminum and copper foils typically used in commercial batteries)[56] to make electrodes. Here, the CF works as both the load-carrying, structural material and the current collector. To study the performance of the CF as a current collector, half cells with CF-based electrodes were tested, and the performance was compared with metal foil-based electrodes.

Using our LTE, we first examined the room-temperature performance of PNTCDI-coated CF electrodes in lithium metal half-cells. A schematic of the half-cell setup is shown in Fig. S4. Fig. 2a shows a typical CV of the half-cell for which PNTCDI showed two oxidation/reduction peaks, indicating a two-step charge transfer reaction mechanism (Fig. S5). From the CV results, the potentials of the reduction (lithiation) peaks were around 2.29 V and 2.54 V (*vs.* Li$^+$/Li), and the potentials of the oxidation (delithiation) peaks were around 2.58 V and 2.72 V (*vs.* Li$^+$/Li). The $E_{1/2}$ of PNTCDI was around 2.43 V for the first peak and 2.63 V for the second peak. Galvanostatic charge–discharge testing (GCD) was applied to determine the capacity at varying C-rates, Fig. 2b. The theoretical capacity of PNTCDI is 158 mAh g^{-1}.[45] At 1C (158 mA g^{-1}) the half-cell exhibited a capacity of 117 mAh g^{-1}, and at 10C (1580 mA g^{-1}) the capacity was 78 mAh g^{-1}. These capacities are 74 and 49% of the theoretical capacity of PNTCDI. Fig. 2c shows the charge/discharge curves for the half-cell, and Fig. S6 and S7 show that these curves are largely similar for both the CF support and the metal foil current collector. These results show that PNTCDI is a suitable negative electrode for the proposed dual-ion battery.

As for the positive electrode, our prior work demonstrated the suitability of PTMA-*co*-GMA-coated CF as a positive electrode, but only at room temperature using 1 M $LiPF_6$ in EC/DEC (1 : 1).[24] In Fig. S8–11, we show that the same electrode is compatible with the LTE at room temperature and that the CF support performs similarly to an aluminum current collector. In Fig. S7, the CV shows one peak, which indicates the redox mechanism of N–O$^\bullet$ radical being oxidized to N=O$^+$ (oxoammonium cation) and *vice versa*. The CV in Fig. S7 shows that the potential of the oxidation peak is 3.95 V (*vs.* Li$^+$/Li), and the potential of the reduction peak is 3.75 V (*vs.* Li$^+$/Li). The $E_{1/2}$ is around 3.85 V. In Fig. S8, the results of GCD testing showed that the half-cell delivered 83 mAh g^{-1} at 1C (110 mA g^{-1}) and

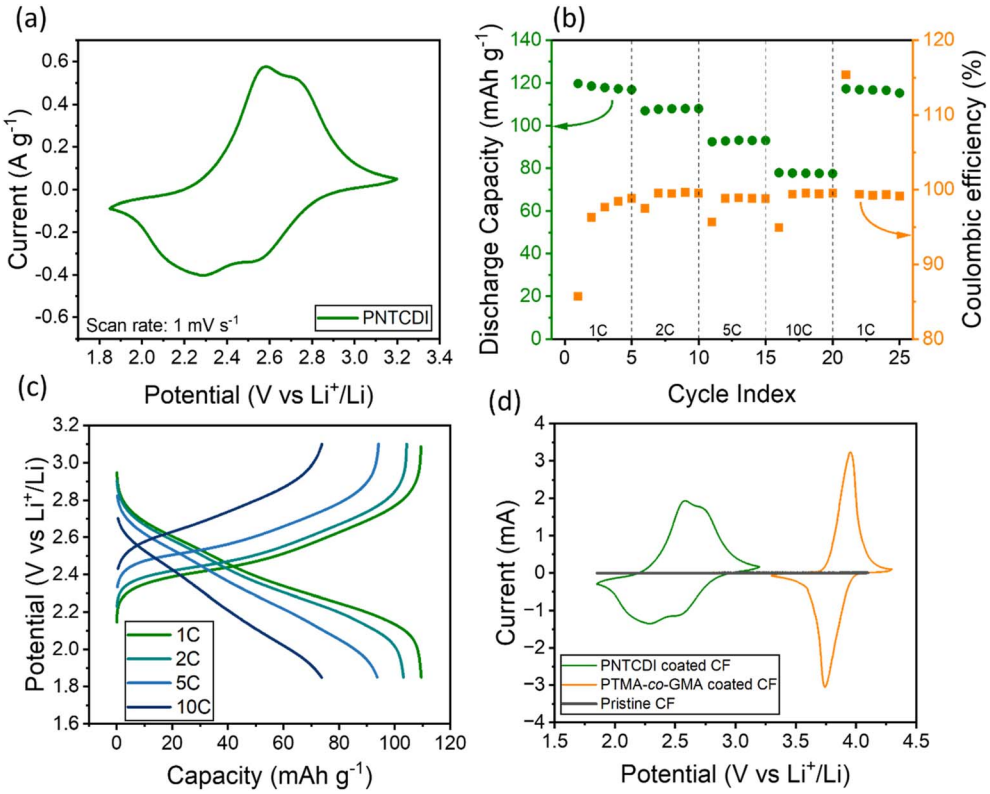

Fig. 2 Electrochemical characteristics of PNTCDI-coated CF in a half cell (*vs.* lithium foil) at room temperature (24 °C). (a) CV at 1 mV s^{-1}. (b) Discharge capacity at varying C-rates. (c) GCD curves at different C-rates. (d) CV curves of PNTCDI, PTMA-*co*-GMA, and neat CF shown together. The electrolyte was 1 M LiTFSI in diglyme/FEC (9 : 1, w : w). All cells had an active material loading of >1 mg cm^{-2}.

58 mAh g^{-1} at 10C, which are about 75% and 53% of the theoretical capacity, respectively.

With our ultimate goal of assembling and evaluating a full cell, we next compared the CV responses of both PNTCDI and PTMA-*co*-GMA-coated CF in their respective lithium metal half cells, Fig. 2d. We also compared the CV response of a neat CF in a lithium metal half-cell; no peaks were observed in the CV for the relevant potential windows, which implies that the CF does not undergo electrochemical reactions in the potential window investigated. Therefore, all of the capacity is delivered by the PNTCDI and the PTMA-*co*-GMA active materials.

Fig. 3 shows the working mechanism of the full cell in this work. Fig. 4a shows CVs of the PNTCDI||PTMA-*co*-GMA full cells. CF-based cells and metal foil-based cells showed almost the same CV shape. Specifically, the full cells exhibited oxidation peaks at 1.5 V and reduction peaks at 1.4 V. The discharge capacities of the CF-based full cell at different C-rates are shown in Fig. 4b. At 1C current (110 mA g^{-1}), the CF-based full cell showed a capacity of 71 mAh g^{-1}. When the charge/discharge current was increased to 10C, the CF-based cell showed a capacity of 58 mAh g^{-1}. Fig. 4c shows the galvanostatic charge/discharge curves at 1C of both CF- and metal foil-based full cells, which display a plateau between 1.2 V and 1.6 V with an average discharge voltage of 1.4 V. Long-term cycling was performed to test the stability of the CF-based-full cell. Charge–discharge cycling at 5C current (550 mA g^{-1}) was performed 300 times and the results are shown in Fig. 4d. After 300 cycles of charge discharge, the CF-based cell exhibited a capacity retention of 91%. The detailed GCD curves are displayed in Fig. 4e.

As for the metal foil-based cells, they showed similar CV shapes, working potentials, and charge/discharge capacities as the CF-based ones. However, the CF-based cells showed superior long term cycling stability. The metal foil-based cells only

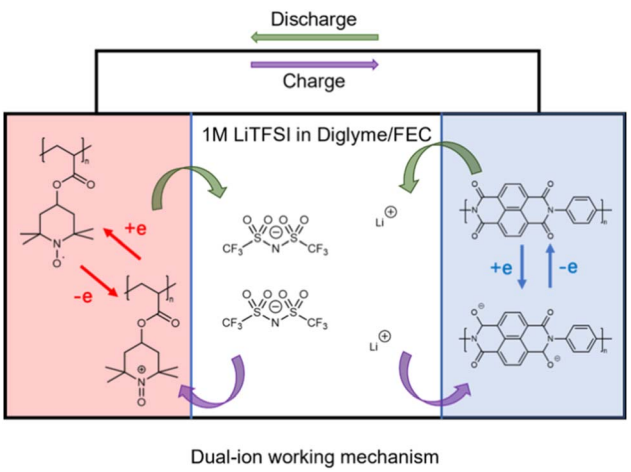

Fig. 3 A schematic diagram of the working mechanism of the full cell in this work.

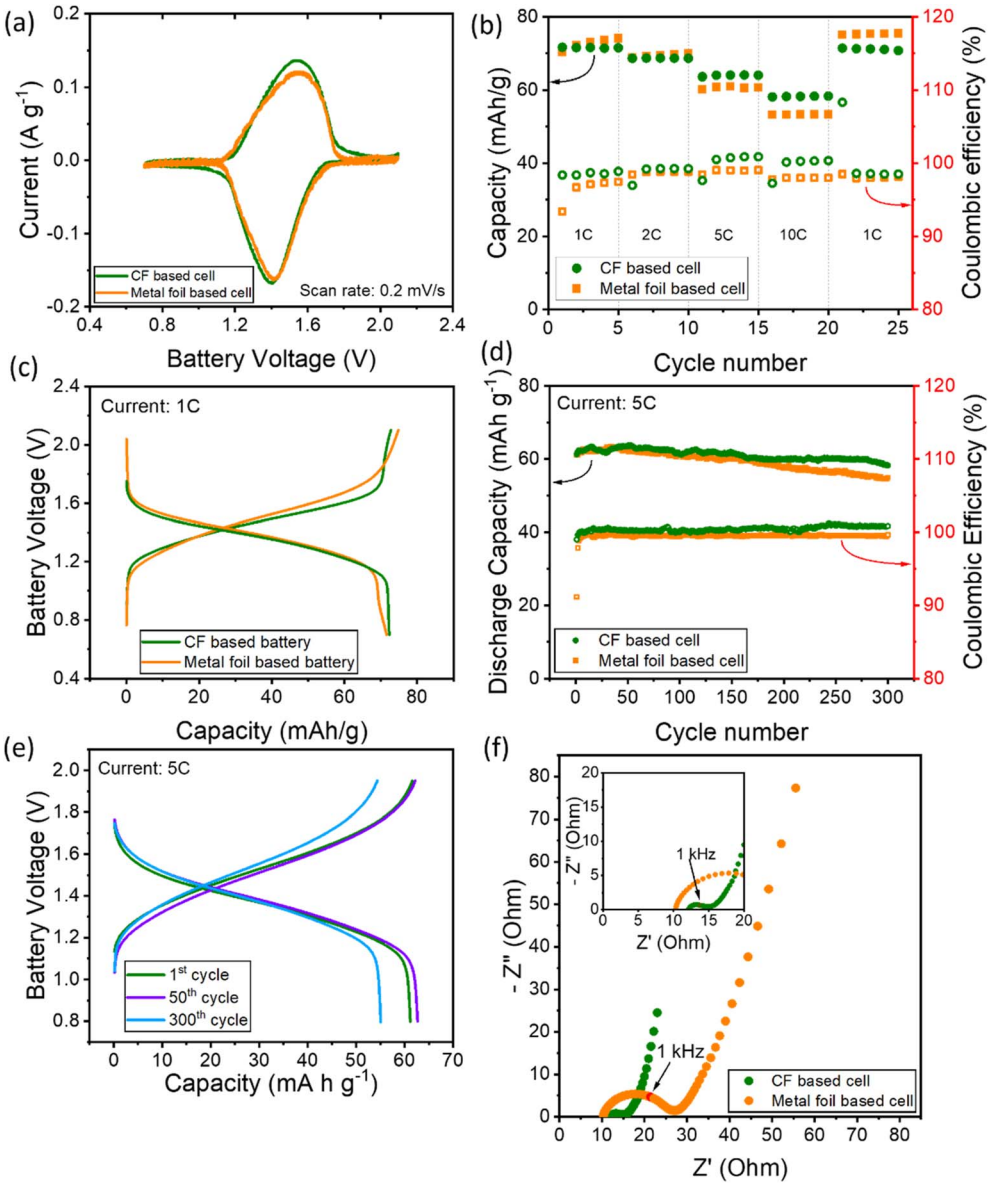

Fig. 4 PNTCDI||PTMA-*co*-GMA full cell characteristics. (a) CV of the full cell using CF weave and metal foil current collectors (scan rate = 0.2 mV s^{-1}). (b) Discharge capacity of the CF-based full cell. (c) GCD curves (current = 1C, 110 mA g^{-1}) and (d) long-term cycling capacities of the full cells (current = 5C). (e) GCD curves of the 1st, 50th, and 300th cycles in the long-term cycling for the CF-based full cell. (f) EIS Nyquist plot of the full cells. All tests were performed at room temperature (24 °C). The positive electrode composition of the battery was 50% PTMA-*co*-GMA, 40% SuperP, and 10% PVDF; the negative electrode composition was 70% PNTCDI, 20% SuperP, and 10% PVDF. The active material mass loading was at least 1 mg cm^{-2}. The N/P capacity ratio was around 1.1 : 1.

retained 86% of their original capacity after 300 cycles, but the CF-based ones retained 91% (Fig. 4d). This signifies that CF-based cells have better long-term cycling stability, possibly due to better surface interactions between the CF-weave and the coated materials. In support of this, electrochemical impedance spectroscopy (EIS) of the CF-based cells showed a much smaller charge transfer resistance than metal foil ones (Fig. 4f), which we attribute to the higher roughness of the CF current collector and non-covalent interactions between the polymer molecules and the CF's graphitic structure. The increased surface area and rougher nature of the carbon fiber weave provides room for volumetric expansion of the active material during cycling. Overall, these results show that in many cases, CF can provide comparable or better electrochemical performance working as current collectors instead of metal foils. Moreover, CFs are able to carry mechanical loads, allowing these weaves to form the basis of a structural battery system. Specifically, our prior work with PTMA-*co*-GMA on CF identified a Young's modulus of 16 GPa and strength of 320 MPa.[24] We expect that PNTCDI-coated CF electrodes will possess similar mechanical properties.

SEM images of PNTCDI and PTMA-*co*-GMA coated CF electrodes before and after cycling are shown in Fig. 5. In which the morphologies appear mostly the same. Specifically, both

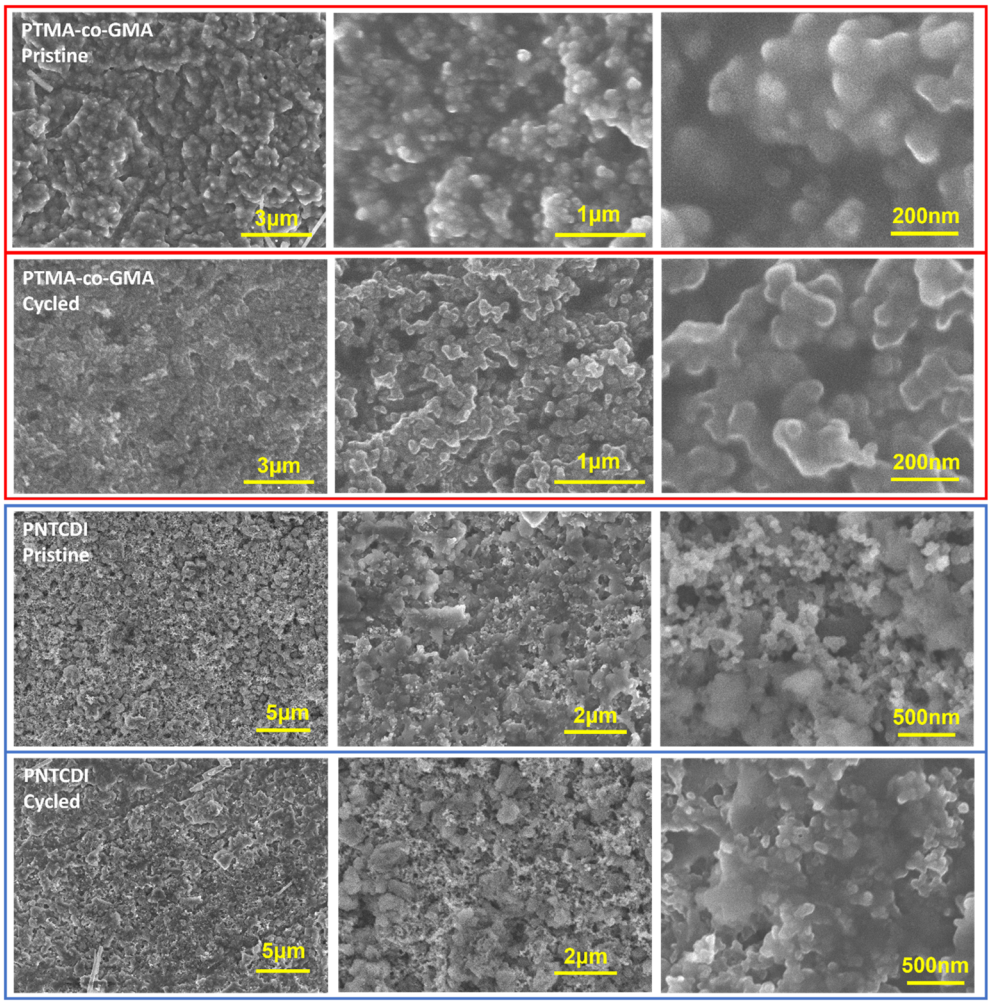

Fig. 5 SEM images of PNTCDI and PTMA-*co*-GMA-coated electrodes before and after cycling at different magnifications, see Fig. 3d. The current collector was CF. The top two rows show PTMA-*co*-GMA structural electrodes; the bottom two show PNTCDI structural electrodes.

PNTCDI and PTMA-*co*-GMA electrodes exhibit a particulate structure attributed to the carbon additive, along with polymer coating the spaces in between. Organic polymer-based batteries work using a conversion mechanism and not an intercalation mechanism,[57] which might explain the absence of obvious changes after cycling. The negligible change in morphology indirectly suggests that the formation of an SEI or CEI is relatively minor. However, prior work suggests the possibility of an interphase formation. Specifically, we previously observed an interphase formation for PTMA-*co*-GMA in the presence of an aqueous electrolyte.[52] Elsewhere, an interphase has been observed for polyimides.[45,58]

The electrochemical performance of the CF-based dual ion batteries cells was assessed at temperatures as low as 0 °C, −10 °C, −20 °C, −30 °C, −40 °C, and −50 °C (Fig. 6a). At 0 °C, the cell showed a capacity of 61 mAh g^{-1}, 59 mAh g^{-1}, 55 mAh g^{-1}, and 45 mAh g^{-1} at 1C, 2C, 5C, and 10C current, respectively. These capacities were about 85% of the room temperature capacity at all equivalent currents. For a constant current of 1C, the discharge capacity of the cell decreased from 58 mAh g^{-1} to 23 mAh g^{-1} as the temperature decreased from −10 °C to −50 °C, respectively. The capacity-decrease from 0 °C to −20 °C was merely 5%. At −50 °C and 1C, the cell delivered a capacity retention of 32%. The galvanostatic charge/discharge curves of the cell at 1C current and various temperatures are given in Fig. 6b. The curves showed that, as the temperature decreases, the polarization of the battery gradually increases. The average discharge plateau voltage remained constant at approximately 1.4 V until −40 °C.

As mentioned before, dual-ion batteries in discharge release ions from the electrodes to the electrolyte. This step is kinetically faster than charging because ion de-solvation in charging has a higher energy barrier than the reverse process. Taking advantage of this, we adjusted our charge–discharge protocol, charging the cell at ambient temperature and then discharging at a low temperature. The cell was first charged at room temperature to 2.1 V and kept at this voltage while the temperature was lowered to a set value. After 1 hour of equilibration, the cell was discharged at −30 °C, −40 °C, and −50 °C. The resulting charge/discharge curves are shown in Fig. 6c. With this charge/discharge method, the cell's discharge capacity increased to 57 mAh g^{-1}, 51 mAh g^{-1}, and 40 mAh g^{-1}

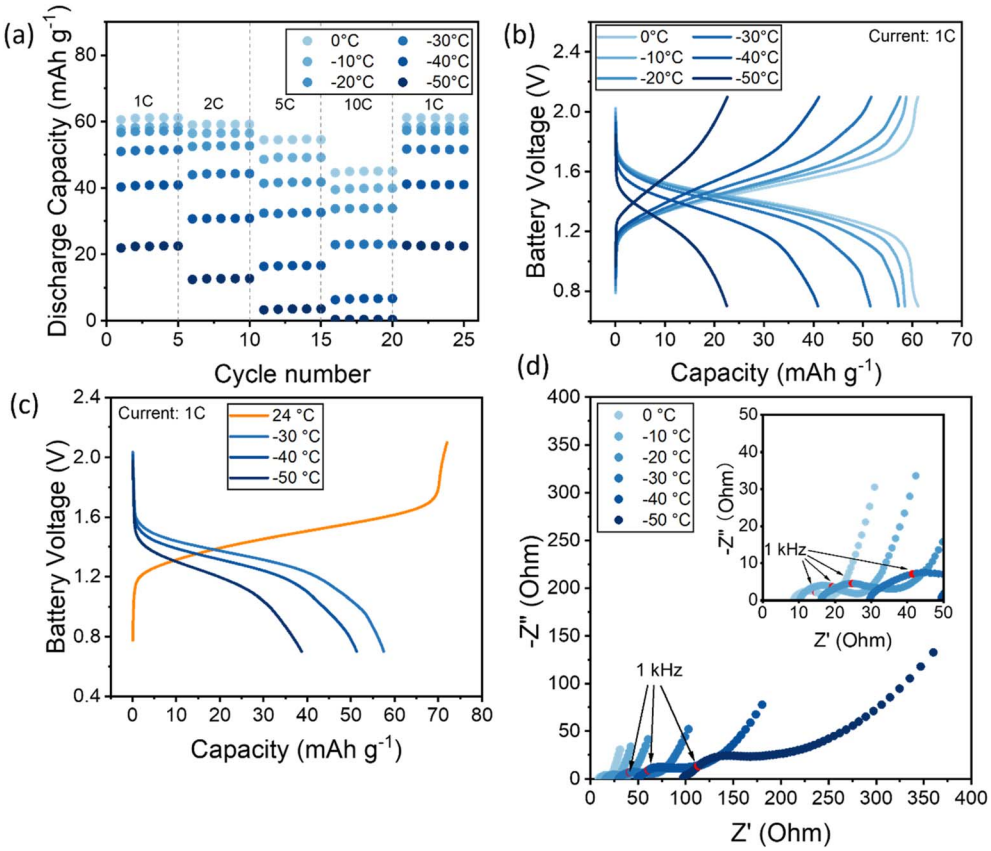

Fig. 6 PNTCDI||PTMA-*co*-GMA full cell characteristics at low temperatures from −50 °C to 0 °C (a) discharge capacity at current from 1C (110 mA g^{-1}) to 10C (1100 mA g^{-1}). (b) GCD profiles of the cell at 1C. (c) GCD curves for the cell battery charged at room temperature, kept at 2.1 V while cooling down, and then discharged at various low temperatures. (d) EIS Nyquist plot of the full cell at different temperatures.

at −30 °C, −40 °C, and −50 °C, respectively. The results show that charging at room temperature and discharging at low temperatures increases the discharge capacity by about 12–74%, depending on discharge temperature. The higher capacity retention of this method proves that dual-ion batteries are suitable to work as low-temperature batteries because they have lower kinetic barriers in discharge.

EIS was performed at different temperatures to study the possible reasons for the capacity decrease at low temperatures (Fig. 6d). The overall impedance of the cell increased as the temperature decreased. The bulk resistance showed a notable increase from ∼10 Ohm to ∼100 Ohm as the temperature decreased to −50 °C. This increase in the resistance is attributed to a decrease in the conductivity of the electrolyte.

For the battery to work well in low-temperature conditions, stability is another important factor. Long-term cycling tests were carried out to determine the capacity decay in low-temperature conditions. The dual-ion cell was subjected 300 cycles at 1C (110 mA g^{-1}) current and −20 °C, (Fig. 7a). The capacity increased in the first few cycles as electrolyte penetrated and activated the polymer electrodes, a process termed "conditioning". After which, little-to-no capacity decay was observed. The GCD curves for the first, the 50th, and the 300th cycles are shown in Fig. 7b, for which the discharge capacities were 52.4 mAh g^{-1}, 54.4 mAh g^{-1}, and 54.5 mAh g^{-1}, respectively. To further examine the cycling stability at other low temperatures, we applied a different strategy in which the battery was first cycled at −20 °C for 200 cycles, then the battery was cycled at −10 °C, 0 °C, room temperature and −20 °C (Fig. 7c). At −20 °C, the battery again showed little-to-no capacity decay. As the temperature increased to 0 °C, capacity decay was evident (0.9% capacity decay after 100 cycles). At room temperature, capacity decay was 4.7% after 100 cycles. At the final set of cycles at −20 °C, the capacity stabilized but did not recover to its original value. Fig. 7d shows the corresponding GCD curves for three different cycles at −20 °C (100th, 200th, and the final cycle 600th). The GCD curves for the final cycle at each different temperature are shown in Fig. 7e. Taken together, this behavior indicates that processes usually associated with degradation in organic batteries (*e.g.* active material dissolution or side reactions) are unfavorable at lower temperatures, thus promoting a higher cycle life.

The energy and power of the dual-ion battery is summarized in a Ragone plot (Fig. 8a and Table S2). For a specific temperature, the energy decreases slightly with increasing C-rate and the power increases significantly. As temperature decreases, both specific power and specific energy decrease. Overall, these results show that the battery can operate at high C-rates even at

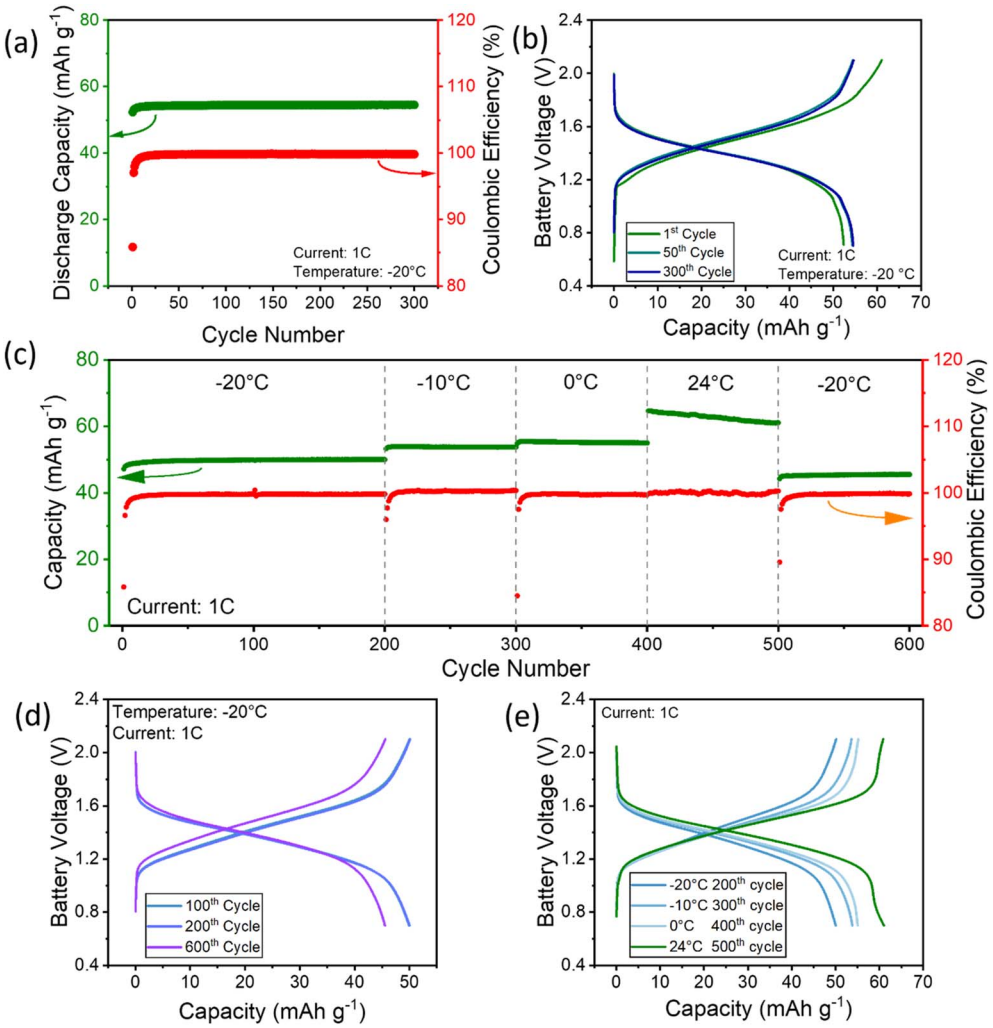

Fig. 7 Long-term cycling results of PNTCDI||PTMA-*co*-GMA full cells. (a) Discharge capacity of the cell cycled at −20 °C and 1C (110 mAh g^{-1}) for 300 cycles. (b) GCD curves of the cell cycled at −20 °C and 1C. (c) The discharge capacity of the cell cycled at different temperatures and 1C current. The GCD curves are also shown in (d) – all taken at −20 °C but different cycle numbers; (e) the last cycle of the GCD curves taken at different temperatures from −20 °C to 24 °C.

low temperatures. Specifically, we observed a power of about 1000 W kg^{-1} at −40 °C, which is significantly higher than competing inorganic batteries (less than 100 W kg^{-1}), discussed below. The reason for this could be attributed to the working mechanism of the organic polymer active materials, which tend to be slightly swollen with electrolyte, allowing for fast ion motion and charge transfer kinetics *versus* intercalation-like typical inorganic materials. To compare our results with the few reports of low-temperature organic batteries, we plotted the maximum specific energy *vs.* temperature in Fig. 8b. Our work is comparable with these other low temperature organic batteries. More importantly, the average working potential of the battery in our work is around 1.4 V, which is higher than that reported by Dong *et al.* in ref. 36 (∼1.2 V) or by Jiang *et al.* in ref. 37 (less than 1 V). This higher working voltage is attributed to the use of PTMA cathode material *in lieu* of the PTPAn material. For the calcium-based battery, it exhibited 9.7% capacity decay after being cycled 450 times at −30 °C,[37] but our dual-ion cell showed negligible capacity fade after cycling 300 times at −20 °C. The superior surface contact and cycling stability of CF current collectors could be contributing to the low capacity fade. Most importantly, the batteries in our work are structurally stiff from the inclusion of CF, whereas the batteries reported in other works were not structural.

Finally, a Ragone plot comparing recent low-temperature battery works, including organic batteries and inorganic batteries is shown in Fig. 8c, with details in Table S3.[36,37,59–62] Studies on low-temperature inorganic batteries typically use traditional metal oxides and graphite materials while altering the electrolyte. The organic and inorganic batteries works are classified into two "regions". Inorganic batteries typically have high specific energy and low specific power. Organic batteries, on the other hand, have high specific power but relatively lower specific energy.[59–62] At low temperatures, organic batteries demonstrate superior power (about 3–10 times higher) in comparison to inorganic ones.

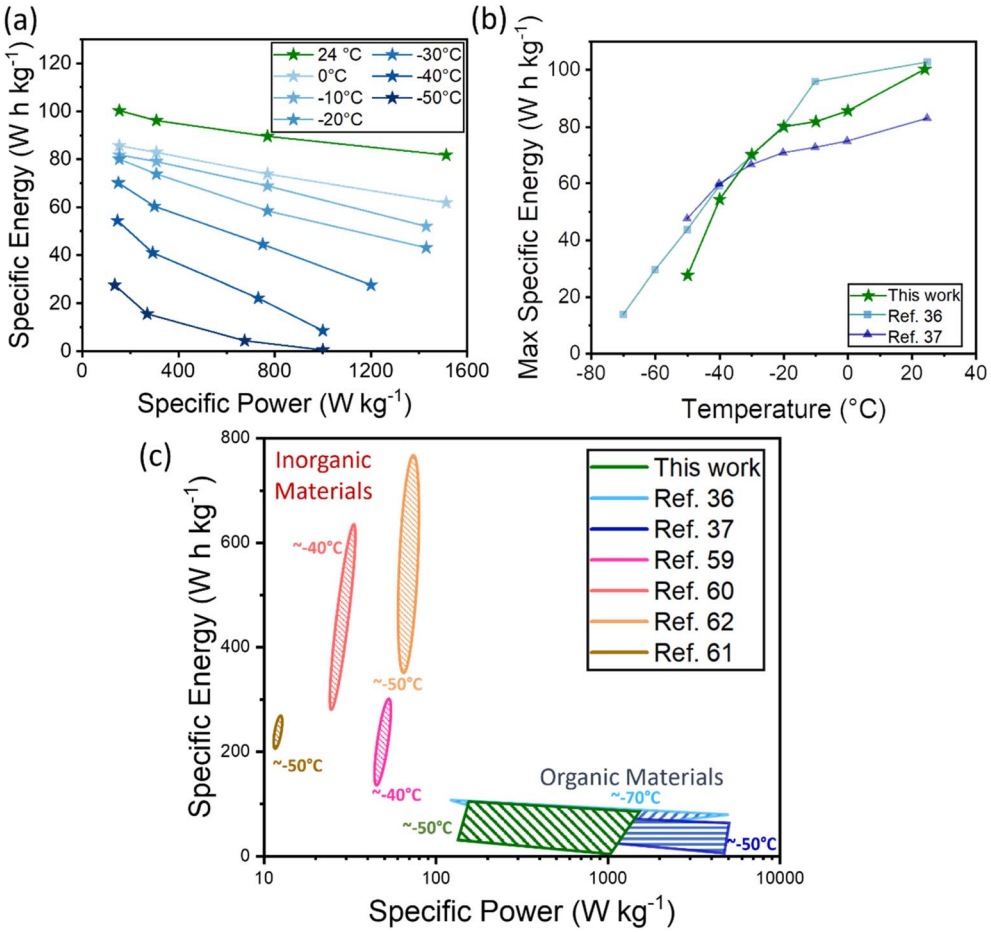

Fig. 8 (a) Ragone plot of the dual-ion battery of this work at different temperatures from −50 °C to room temperature. (b) Maximum specific energy *vs.* temperature plot for this work and two others.[36,37] (c) Ragone plot of recent low-temperature batteries.[36,37,59–62] Organic batteries at low temperatures show a specific power that is roughly 3–10 times higher than inorganic ones at maximum specific energy.

4. Conclusion

In this work, we demonstrated a dual-ion battery with both structural properties and low-temperature operability, utilizing PNTCDI and PTMA-*co*-GMA coated CF as electrodes with LiTFSI/diglyme-based low-temperature electrolyte. CF showed similar electrochemical performance as metal foil current collectors, showing their potential for replacement. We expect that, in future applications in structural batteries, CF as current collectors will give load-bearing capabilities as they are incorporated into the electrode itself. Using a low-temperature electrolyte and a dual-ion configuration, the cells herein maintained 85% of the room temperature capacity at 0 °C and 55% capacity at −40 °C. Surprisingly, we found that the cells experienced little-to-no capacity decay while cycling at low temperatures, which we attribute to reduced or delayed degradation. A particular highlight of this cell is the high power obtained (about 1000 W kg^{-1} at −40 °C), which is significantly higher than competing inorganic batteries (over 10 times). Coupled with high mechanical strength CF current collectors, the low-temperature operable battery configuration has the potential to expand the multifunctionality of batteries and meet the needs of power storage in harsh environments. Future work will focus on increasing the voltage, capacity, and specific energy of the dual-ion cell and the conductivity of the electrolyte at lower temperatures.

Author contributions

The manuscript was written through the contributions of all authors. All authors have given approval to the final version of the manuscript.

Conflicts of interest

The authors declare no conflict of interest.

Data availability

The data supporting this article have been included as part of the SI.

Melting points and boiling points of electrolyte solvents. EPR spectrum of PTMA-*co*-GMA. FTIR spectrum of PNTCDI. A schematic diagram of a PNTCDI//lithium foil half-cell. CV of

a PNTCDI-coated carbon fiber half-cell. CV of a PNTCDI-coated copper foil half-cell. The discharge capacity and coulombic efficiency of PNTCDI coated copper foil half-cell CV of PTMA-*co*-GMA-coated carbon fiber half-cell with redox mechanism. The discharge capacity and coulombic efficiency of PTMA-*co*-GMA coated carbon fiber half-cell. CV of PTMA-*co*-GMA-coated aluminum foil half-cell. The discharge capacity and coulombic efficiency of PTMA-*co*-GMA coated aluminum foil half-cell. Molecular characterization of PNTCDI *via* solid state ^{13}C NMR spectrum. Table of specific energies and specific powers. See DOI: **https://doi.org/10.1039/d5ta01626f**.

Acknowledgements

This work was supported by the Air Force Office of Scientific Research Grant No. FA9550-22-1-0388. The authors also thank Dr Yordanos Bisrat (Texas A&M University Materials Characterization Core Facility (RRID: SCR_022202)) for assistance with top-down SEM imaging. C. Wang prepared the original draft; Dr J. L. Lutkenhaus reviewed and edited the article; C. Wang synthesized the PTMA-*co*-GMA and PNTCDI, prepared the electrodes and batteries used in experiments, and performed electrochemical tests including tests under varied temperatures. S. S. Oka performed SEM imaging. M. Avais performed solid state NMR. The authors declare no competing financial interests. All authors approved the final manuscript. Snowflake image in the graphical abstract is by Janek Lass under CC BY 4.0 licence (**https://creativecommons.org/licenses/by/4.0/**)

References

1 A. Gupta and A. Manthiram, *Adv. Energy Mater.*, 2020, **10**, 2001972.
2 R. Chaudhary, J. Xu, Z. Xia and L. E. Asp, *Adv. Mater.*, 2024, **36**(48), 2409725.
3 L. E. Asp, M. Johansson, G. Lindbergh, J. Xu and D. Zenkert, *Funct. Compos. Struct.*, 2019, **1**, 042001.
4 P. Flouda, S. Oka, D. Loufakis, D. C. Lagoudas and J. L. Lutkenhaus, *ACS Appl. Mater. Interfaces*, 2021, **13**, 34807–34817.
5 Y. Feng, L. Zhou, H. Ma, Z. Wu, Q. Zhao, H. Li, K. Zhang and J. Chen, *Energy Environ. Sci.*, 2022, **15**, 1711–1759.
6 Y. Li, Y. Zheng, K. Guo, J. Zhao and C. Li, *Adv. Energy Mater.*, 2022, **2022**, 9840837.
7 J. Tian, D. Cao, X. Zhou, J. Hu, M. Huang and C. Li, *ACS Nano*, 2018, **12**, 3424–3435.
8 D. Pandey, K. Sambath Kumar, L. N. Henderson, G. Suarez, P. Vega, H. R. Salvador, L. Roberson and J. Thomas, *Small*, 2022, **18**, 2107053.
9 W. Chen, J. Liang, Z. Yang and G. Li, *Energy Procedia*, 2019, **158**, 4363–4368.
10 H. Zhou, H. Li, L. Li, T. Liu, G. Chen, Y. Zhu, L. Zhou and H. Huang, *Mater. Today Energy*, 2022, **24**, 100924.
11 L. E. Asp and E. S. Greenhalgh, *Compos. Sci. Technol.*, 2014, **101**, 41–61.
12 J. Snyder, R. Carter, E. Wong, P. Nguyen, K. Xu, E. Ngo and E. Wetzel, *International SAMPE Technical Conference*, 2007, vol. 18.
13 S. Deshpande, V. Vidyaprakash, S. Oka, S. S. Dasari, K.-W. Liu, C. Wang, J. L. Lutkenhaus and M. J. Green, *ACS Appl. Polym. Mater.*, 2024, **6**, 6323–6333.
14 W. Johannisson, D. Zenkert and G. Lindbergh, *Multifunct. Mater.*, 2019, **2**, 035002.
15 J. Yao, J. Xie, K. Nishimura, T. Mukai, T. Takasaki, K. Tsutsumi and T. Sakai, *Ionics*, 2013, **19**, 1849–1853.
16 S. K. Martha, J. O. Kiggans, J. Nanda and N. J. Dudney, *J. Electrochem. Soc.*, 2011, **158**, A1060.
17 J. Hagberg, H. A. Maples, K. S. P. Alvim, J. Xu, W. Johannisson, A. Bismarck, D. Zenkert and G. Lindbergh, *Compos. Sci. Technol.*, 2018, **162**, 235–243.
18 S. Leijonmarck, T. Carlson, G. Lindbergh, L. E. Asp, H. Maples and A. Bismarck, *Compos. Sci. Technol.*, 2013, **89**, 149–157.
19 J. S. Sanchez, J. Xu, Z. Xia, J. Sun, L. E. Asp and V. Palermo, *Compos. Sci. Technol.*, 2021, **208**, 108768.
20 T. Pereira, Z. Guo, S. Nieh, J. Arias and H. T. Hahn, *Compos. Sci. Technol.*, 2008, **68**, 1935–1941.
21 F. Gasco and P. Feraboli, *J. Compos. Mater.*, 2013, **48**, 899–910.
22 H. Lu, J. Hagberg, G. Lindbergh and A. Cornell, *Nano Energy*, 2017, **39**, 140–150.
23 L. E. Asp, K. Bouton, D. Carlstedt, S. Duan, R. Harnden, W. Johannisson, M. Johansen, M. K. G. Johansson, G. Lindbergh, F. Liu, K. Peuvot, L. M. Schneider, J. Xu and D. Zenkert, *Adv. Energy Sustain. Res.*, 2021, **2**, 2000093.
24 S. S. Oka, R. M. Thakur, C. Wang, C. Scrudder, V. Vidyaprakash, D. C. Lagoudas, J. G. Boyd, M. J. Green and J. L. Lutkenhaus, *J. Electrochem. Soc.*, 2024, **171**, 070505.
25 J. Fan, *J. Power Sources*, 2003, **117**, 170–178.
26 S. S. Zhang, K. Xu and T. R. Jow, *J. Power Sources*, 2003, **115**, 137–140.
27 C.-K. Huang, J. S. Sakamoto, J. Wolfenstine and S. Surampudi, *J. Electrochem. Soc.*, 2000, **147**, 2893.
28 Y. Ein-Eli, S. R. Thomas, R. Chadha, T. J. Blakley and V. R. Koch, *J. Electrochem. Soc.*, 1997, **144**, 823–829.
29 E. J. Plichta and W. K. Behl, *J. Power Sources*, 2000, **88**, 192–196.
30 D. Yaakov, Y. Gofer, D. Aurbach and I. C. Halalay, *J. Electrochem. Soc.*, 2010, **157**, A1383.
31 M. C. Smart, B. V. Ratnakumar and S. Surampudi, *J. Electrochem. Soc.*, 1999, **146**, 486–492.
32 M. C. Smart, B. V. Ratnakumar, L. D. Whitcanack, K. B. Chin, S. Surampudi, H. Croft, D. Tice and R. Staniewicz, *J. Power Sources*, 2003, **119–121**, 349–358.
33 K. Xu, *Chem. Rev.*, 2004, **104**, 4303–4418.
34 Y. X. Yao, N. Yao, X. R. Zhou, Z. H. Li, X. Y. Yue, C. Yan and Q. Zhang, *Adv. Mater.*, 2022, **34**, 2206448.
35 J. Xu, X. Wang, N. Yuan, J. Ding, S. Qin, J. M. Razal, X. Wang, S. Ge and Y. Gogotsi, *Energy Storage Mater.*, 2019, **23**, 383–389.
36 X. Dong, Z. Guo, Z. Guo, Y. Wang and Y. Xia, *Joule*, 2018, **2**, 902–913.

37 B. Jiang, Y. Su, R. Liu, Z. Sun and D. Wu, *Small*, 2022, **18**, 2200049.
38 K. Nakahara, S. Iwasa, M. Satoh, Y. Morioka, J. Iriyama, M. Suguro and E. Hasegawa, *Chem. Phys. Lett.*, 2002, **359**, 351–354.
39 J. Kim, J. H. Kim and K. Ariga, *Joule*, 2017, **1**, 739–768.
40 S. Muench, A. Wild, C. Friebe, B. Häupler, T. Janoschka and U. S. Schubert, *Chem. Rev.*, 2016, **116**, 9438–9484.
41 N. Patil, A. Aqil, F. Ouhib, S. Admassie, O. Inganäs, C. Jérôme and C. Detrembleur, *Adv. Mater.*, 2017, **29**, 1703373.
42 T. Ma, A. D. Easley, R. M. Thakur, K. T. Mohanty, C. Wang and J. L. Lutkenhaus, *Annu. Rev. Chem. Biomol. Eng.*, 2023, **14**, 187–216.
43 J.-K. Kim, G. Cheruvally, J.-H. Ahn, Y.-G. Seo, D. S. Choi, S.-H. Lee and C. E. Song, *J. Ind. Eng. Chem.*, 2008, **14**, 371–376.
44 S. Wang, A. M. G. Park, P. Flouda, A. D. Easley, F. Li, T. Ma, G. D. Fuchs and J. L. Lutkenhaus, *ChemSusChem*, 2020, **13**, 2371–2378.
45 Z. Song, H. Zhan and Y. Zhou, *Angew. Chem., Int. Ed.*, 2010, **49**, 8444–8448.
46 L. Zhang, H. Wang, X. Zhang and Y. Tang, *Adv. Funct. Mater.*, 2021, **31**, 2010958.
47 X. Lei, Y. Zheng, F. Zhang, Y. Wang and Y. Tang, *Energy Storage Mater.*, 2020, **30**, 34–41.
48 Y. Tong, Y. Wei, A. Song, Y. Ma and J. Yang, *ChemSusChem*, 2024, **17**, e202301468.
49 Z. Li, Y. Zhang, J. Zhang, Y. Cao, J. Chen, H. Liu and Y. Wang, *Angew. Chem., Int. Ed.*, 2022, **61**, e202116930.
50 S. Tobishima, H. Morimoto, M. Aoki, Y. Saito, T. Inose, T. Fukumoto and T. Kuryu, *Electrochim. Acta*, 2004, **49**, 979–987.
51 Z. Li, Y. X. Yao, S. Sun, C. B. Jin, N. Yao, C. Yan and Q. Zhang, *Angew. Chem., Int. Ed.*, 2023, **62**, e202303888.
52 R. Mitra Thakur, T. Ma, G. Shamblin, S. S. Oka, S. M. Lalwani, A. D. Easley and J. L. Lutkenhaus, *ChemSusChem*, 2024, **17**, e202400788.
53 X. Zhang, R. Kostecki, T. J. Richardson, J. K. Pugh and P. N. Ross, *J. Electrochem. Soc.*, 2001, **148**, A1341.
54 M. Egashira, H. Takahashi, S. Okada and J.-i. Yamaki, *J. Power Sources*, 2001, **92**, 267–271.
55 N. Chang, T. Li, R. Li, S. Wang, Y. Yin, H. Zhang and X. Li, *Energy Environ. Sci.*, 2020, **13**, 3527–3535.
56 P. Zhu, D. Gastol, J. Marshall, R. Sommerville, V. Goodship and E. Kendrick, *J. Power Sources*, 2021, **485**, 229321.
57 M. Jiang, D. L. Danilov, R. A. Eichel and P. H. L. Notten, *Adv. Energy Mater.*, 2021, **11**, 2103005.
58 S. Liu, T. Kong, S. Xu, R. Xiao and X. Ke, *Nano Lett.*, 2024, **24**, 14168–14175.
59 Y. Yang, Y. Chen, L. Tan, J. Zhang, N. Li, X. Ji and Y. Zhu, *Angew. Chem., Int. Ed.*, 2022, **61**, e202209619.
60 H. Hu, J. Li, Q. Zhang, G. Ding, J. Liu, Y. Dong, K. Zhao, M. Yu, H. Wang and F. Cheng, *Chem. Eng. J.*, 2023, **457**, 141273.
61 X. Dong, Y. Yang, B. Wang, Y. Cao, N. Wang, P. Li, Y. Wang and Y. Xia, *Adv. Sci.*, 2020, **7**, 2000196.
62 J. Xu, J. Zhang, T. P. Pollard, Q. Li, S. Tan, S. Hou, H. Wan, F. Chen, H. He, E. Hu, K. Xu, X.-Q. Yang, O. Borodin and C. Wang, *Nature*, 2023, **614**, 694–700.